Effects of defect structures at surfaces and thin films on grazing scattering of fast ions

R. Pfandzelter*
Humboldt-Universität zu Berlin, Institut für Physik, Invalidenstrasse 110, 10115 Berlin, Germany
(Received 18 September 1997; revised manuscript received 3 December 1997)

Studies on grazing scattering of 25 keV H^+ and He^+ ions from clean Fe(001) and submonolayer films of Cr and Mn on Fe(001) are reported. We find that angular distributions of reflected ions directly depend on the defect structure of the topmost surface layer. Surface defects of different dimensions (thermal displacements, surface steps, islands) can be separated due to characteristic effects on the scattering process. Computer simulations based on the binary collision approximation permit a quantitative analysis of data.
[S0163-1829(98)04524-X]

I. INTRODUCTION

Real single crystal surfaces always have defects. These defects may be zero, one, or two dimensional.[1] Zero-dimensional defects are point defects at single lattice sites. An example are thermal displacements of lattice atoms, which are inevitable. One-dimensional defects may be formed by atomic steps. These are produced to some extent during surface preparation. Boundaries of islands which nucleate on the surface during epitaxial growth belong also to this class, although the islands themselves may be regarded as two-dimensional defects.

In this work we discuss the effect of surface defects on the scattering of fast light ions, which are incident at a grazing angle upon a single crystal surface. The ions are steered by the repulsive interaction potentials with target atoms and reflected in front of the topmost surface layer. Ion-surface interaction may be studied from a number of experimental observables such as energy loss, charge state or secondary emission (see, e.g., Refs. 2 and 3). The most direct effect of surface defects on the scattering process, however, is probably on the angular distribution of reflected ions.

Scattering of fast ions can be treated within the framework of classical mechanics.[4,5] In the case of a smooth, defect-free surface the scattering process may be described in terms of a ''semiplanar surface channeling'': the ions do not interact with individual target atoms but are steered by a planar continuum potential which results from an averaging over the interaction potentials along the surface plane. The trajectories are then obtained by a one-dimensional integration of Newton's equation of motion. The presence of a surface corrugation or surface defects, however, breaks the symmetry and requires a treatment of the scattering in three dimensions. This may be achieved by classical models for particle-surface scattering, such as, e.g., the hard-cube model,[6–8] or three-dimensional trajectory simulations. In computer simulations two main approaches are used:[5,9,10] the molecular dynamics method (MD) and the binary collision approximation (BCA). MD codes solve Newton's equation numerically. The BCA considers a series of successive binary collisions and approximates the trajectory by its asymptotes before and after each collision. MD codes are inherently more reliable, but much more expensive in computer time, and, therefore, inefficient in cases where a large number of trajectories is required for good statistics. Grazing ion-surface scattering has been modeled in a number of MD and BCA calculations,[11–18] which are generally based on atomically flat surfaces.

In the present work we are concerned with the effect of surface defects on the scattering process. We study the scattering of 25 keV H^+ and He^+ ions from clean Fe(001) and submonolayer films of Cr and Mn on Fe(001). Measured polar angular distributions are interpreted by means of computer simulations based on a BCA code.

II. EXPERIMENT

Our experiments on grazing scattering of 25 keV He^+ and H^+ ions from clean Fe(001) and Cr or Mn on Fe(001) have been presented in Refs. 19–22. A well collimated ion beam (maximum angular divergence $\pm 0.02°$) is directed on the target at a polar incidence angle $\Phi_{in}=1.0°-2.0°$ to the surface plane and an azimuthal angle $\Theta_{in}\approx 8°$ to the [100] surface lattice direction. This angle has been found to be large enough to avoid effects due to axial surface channeling (''random azimuthal orientation''). Projectiles scattered in the forward direction within the plane spanned by the ion beam and the surface normal are detected by a channeltron detector. The detector is mounted on a precision manipulator which is moved in the plane of scattering to measure the intensity of scattered projectiles as function of the polar scattering angle Φ_s. A 0.5 mm diaphragm in front of the channeltron defines an angular acceptance of $\pm 0.02°$. The diaphragm is covered by a thin carbon foil for an equal response in the detection of different charge states. For specular reflection holds $\Phi_s=2\Phi_{in}$.

III. COMPUTER SIMULATION

The experiments are simulated by a computer calculation using a lattice program based on the binary collision approximation (BCA). Our program is an adaptation of programs which have been exploited in studies on axial ion-surface channeling.[23,24] The ion beam is simulated by projectiles starting one by one with the same energy of 25 keV. The lattice structure of the semi-infinite Fe(001) crystal is incorporated using a low-index row-oriented procedure. The polar incidence angle Φ_{in} to the (001) surface plane and the azi-

muthal incidence angle Θ_{in} to the [100] direction are taken from the experiment. The starting points are homogeneously distributed within the unit cell of the surface lattice 10 Å above the surface. The trajectory of each projectile is calculated by a series of successive binary collisions with the target atom closest to the instantaneous projectile position. The search of the collision partner is performed by appropriate transformations of the projectile coordinates.

The scattering angle in a binary collision is calculated in the momentum approximation.[25,26] The repulsive interatomic interaction is described by a screened Coulomb potential with the Molière approximation to the Thomas-Fermi screening function[27] and a screening length proposed by O'Connor and Biersack[28] (TFMOB potential). Uncorrelated thermal displacements of target atoms are taken into account using the harmonic model, i.e., by a Gaussian probability density function of the lattice atoms.[29] The mean square displacements $\langle u_z^2 \rangle$ and $\langle u_{x,y}^2 \rangle$ perpendicular and parallel to the surface plane, respectively, are calculated from Debye temperatures T_z and $T_{x,y}$ using the high-temperature approximation

$$\langle u_{x,y,z}^2 \rangle = 3\hbar^2 T / M k T_{x,y,z}^2, \tag{1}$$

where M is the mass of the Fe lattice atom and the other symbols have their usual meanings.[30] For the topmost Fe(001) layer $T_z = 227$ K and $T_{x,y} = 250$ K.[31] Vibrations are assumed to be isotropic for layers beneath the surface with a bulk Debye temperature of 470 K. Equation (1) approximates the exact relation to better than 1% above 300 K for the topmost layer.

In order to test the accuracy of our simulation we calculated the distance of closest approach to the surface z_0 for scattering from a perfect surface without thermal displacements for different incidence angles Φ_{in} of the He^+ ions (Fig. 1, full circles). The incidence angle (right hand ordinate) is given by the transverse energy $E_z = E_0 \sin \Phi_{in}^2$ (kinetic energy for the momentum component of the beam perpendicular to the surface), which transforms at the turning point z_0 to the potential energy given on the left hand ordinate. The simulation yields values for z_0 which agree with results for one-dimensional scattering from a planar continuum potential V_{pl}, where z_0 is given by the condition $E_z = V_{pl}(z_0)$ (Fig. 1, solid curve). This indicates that the scattering process is described properly in the program. In particular, it shows that simultaneous collisions with more than one partner are negligible under the present conditions.

Typical trajectories are presented in Fig. 2 for $\Phi_{in} = 1.75°$ (solid curves). They closely resemble the trajectory obtained from a numerical integration of Newton's equation of motion in the planar continuum potential (dashed curve), although deviations near the turning points are visible, indicating the limited applicability of the continuum approximation. The distance L traveled until the monatomic step height $z_s = 1.433$ Å is reached amounts to 96 Å, and may be defined as interaction length of the projectile with the target surface.

We included in Fig. 1 the planar continuum potentials calculated from the Thomas-Fermi-Molière[27] interatomic potential with Firsov's screening length[33] (TFM) (dashed curve) and the Ziegler-Biersack-Littmark potential[34] (ZBL) (dotted curve). The TFMOB potential closely matches the

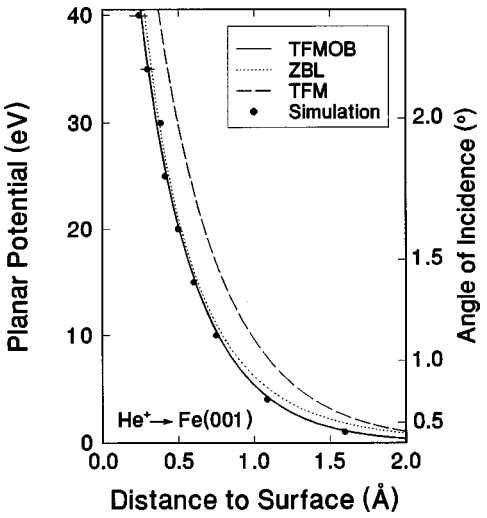

FIG. 1. Planar continuum potentials for scattering of He at Fe(001). The potentials have been calculated from the Thomas-Fermi-Molière interatomic potential (Ref. 27) with a screening length proposed by O'Connor and Biersack (TFMOB) (Ref. 28) and Firsov (TFM) (Ref. 33), respectively, and from the Ziegler-Biersack-Littmark interatomic potential (ZBL) (Ref. 34). The symbols show the distance of closest approach as obtained from the BCA computer simulation. Note that the circles represent average values due to different starting points of the projectiles with respect to the surface lattice. The right hand ordinate gives the incidence angle Φ_{in} for a transverse energy $E_z = E_0 \sin \Phi_{in}^2$ that is equal to the planar potential given on the left hand ordinate (beam energy $E_0 = 25$ keV).

ZBL potential, which is assumed to be the best choice for mean interatomic potentials,[5,28] although there is evidence that it is too strong at large distances.[5,35] Therefore discrepancies between the TFMOB and ZBL potentials at small energies are hard to appraise. Moreover, long-range attractive potentials may drastically affect the scattering at these small transverse energies. This has been predicted by computer simulations for chemisorptionlike[36] and image potentials[37] and verified experimentally.[38–40]

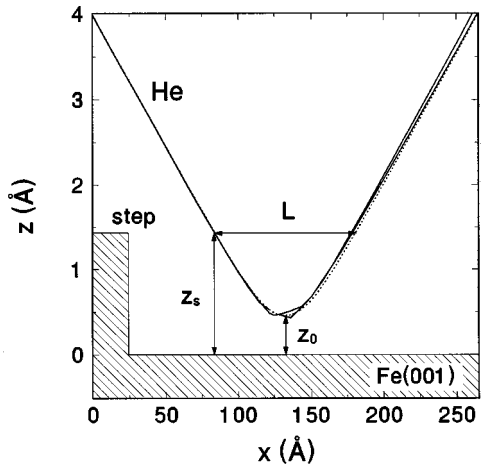

FIG. 2. Simulated trajectories for 25 keV He^+ ions scattered from a perfect rigid Fe(001) surface (solid curves), and trajectory obtained from a numerical integration of Newton's equation of motion in the planar continuum potential (Ref. 32) (dashed curve). Incidence angle $\Phi_{in} = 1.75°$.

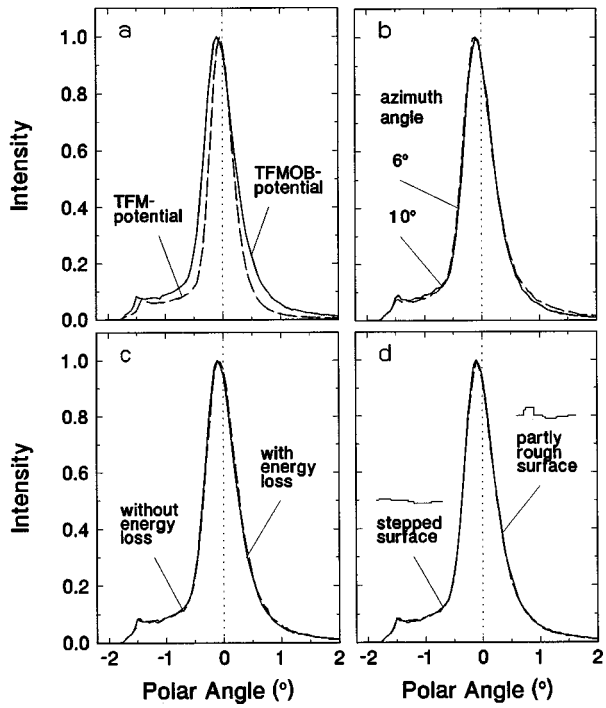

FIG. 3. Calculated polar angular distributions for 25 keV He^+ ions scattered from Fe(001). Incidence angle $\Phi_{in}=1.75°$, temperature $T=600$ K, mean distance between steps $s=500$ Å. (a) TFMOB potential (solid curve), TFM potential (dashed curve). (b) Azimuthal incidence angle to [100] direction $\Theta_{in}=6°$ (solid curve) and 10° (dashed curve), respectively. (c) Without (solid curve) and with (dashed curve) energy loss, respectively. (d) 5% of the incident ions hit a rough surface area (dashed curve). The dotted vertical lines indicate specular reflection ($\Phi=\Phi_s-2\Phi_{in}=0°$).

Computer simulations of ion-solid scattering inherently contain approximations due to limited computational power and, in particular, the lack of an exact physical description of the processes involved. Therefore it must be the aim of a computational approach to identify the influence of the physical parameters, in order to achieve a sufficiently realistic description of the scattering experiment with a minimum number of physical processes and quantities considered. Figure 3 shows typical polar angular distributions simulated for scattering of He^+ from an Fe(001) surface with surface steps and thermal displacements (see Sec. IV). The distributions show a narrow, nearly Gaussian peak centered slightly below the angle for specular reflection and a foot at smaller scattering angles (for convenience we plot, as abscissa, the polar angle $\Phi=\Phi_s-2\Phi_{in}$). Though it is not surprising that the choice of interatomic potential has some influence on the angular distribution, the gross features are not affected [Fig. 3(a)]. The azimuthal angle of incidence is varied in Fig. 3(b) between $\Theta_{in}=6°$ (solid curve) and 10° (dashed curve). No influence is observed, in accord with our experimental observation (see, e.g., Ref. 21).

So far we have considered only *elastic* scattering. *Inelastic* processes (phonon, plasmon, electron-hole pair excitation) have been neglected. These processes lead to nuclear and electronic energy loss of the projectiles. Because nuclear energy transfer is negligible in grazing scattering,[41] the total energy loss is determined by electronic excitations. We tentatively incorporate electronic energy loss using the velocity- and electron-density-dependent stopping power as obtained from nonlinear density-functional calculations (curve E in Ref. 42) and the local conduction-electron density above the Fe(001) surface from Ref. 43. Between two successive collisions the resulting three-dimensionally position-dependent stopping power is integrated along the path of the projectile and subtracted from the projectile energy. For the conditions used in Fig. 3 the mean energy loss of scattered projectiles is computed to 630 eV (2.5% of the beam energy), which roughly corresponds to measured energy losses for scattering of He from metal surfaces.[44] The effect of energy loss on the scattering process is negligible here, as shown in Fig. 3(c). The same holds for multiple scattering by surface electrons. Incorporation into the simulation using the momentum approximation in ion-electron collisions[45] does not show effects on the polar angular distributions.

In studies on grazing ion-surface scattering it is common to implicitly assume surfaces consisting of extended flat terraces separated by surface steps with atomic-scale heights. Yet macroscopic surfaces may have regions with large protrusions or depressions due to, e.g., grain boundaries or mechanical damage during preparation. This often does not seriously affect the outcome of experiments, as can be seen from Fig. 3(d). The dashed curve is the result of a calculation, where 5% of the incident projectiles hit a rough surface region, modelled by 100 Å high steps. These particles do not show correlated small angle scattering, i.e., they do not appear at angles within the polar angular distributions studied here.

In conclusion, polar angular distributions can be adequately simulated by elastic scattering in a three-dimensional repulsive potential. Inelastic processes, which are difficult to implement in a realistic way, may be neglected. For very small transverse energies ($\approx$eV) we see general problems owing to the insufficient knowledge of relevant repulsive and attractive potentials.

Our simulations are performed on a DEC3000 workstation. 10^6 trajectories are followed for a polar angular distribution, which requires typically 1 h in elapsed time. Incorporation of, e.g., energy loss or multiple scattering increases this time considerably.

IV. RESULTS AND DISCUSSION

A. Surface steps

A measured polar angular distribution is shown in Fig. 4(a) (circles) for scattering of 25 keV He^+ ions at $\Phi_{in}=1.75°$ and $T=600$ K. The curves are results of the computer simulation. For a perfect and rigid surface the calculated distribution consists of an almost δ-shaped peak at $\Phi=\Phi_s-2\Phi_{in}=0°$, i.e., all projectiles are specularly reflected as it is expected from the concept of ''semiplanar surface channeling.'' Inclusion of thermal vibrations clearly broadens the distribution. This broadening shows the same asymmetry as in the experimental data; the maximum shifts to smaller angles (''subspecular reflection'') and a tail evolves for larger scattering angles. The broadening is caused by the thermal displacement component perpendicular to the surface; parallel components turned out to be of minor importance.

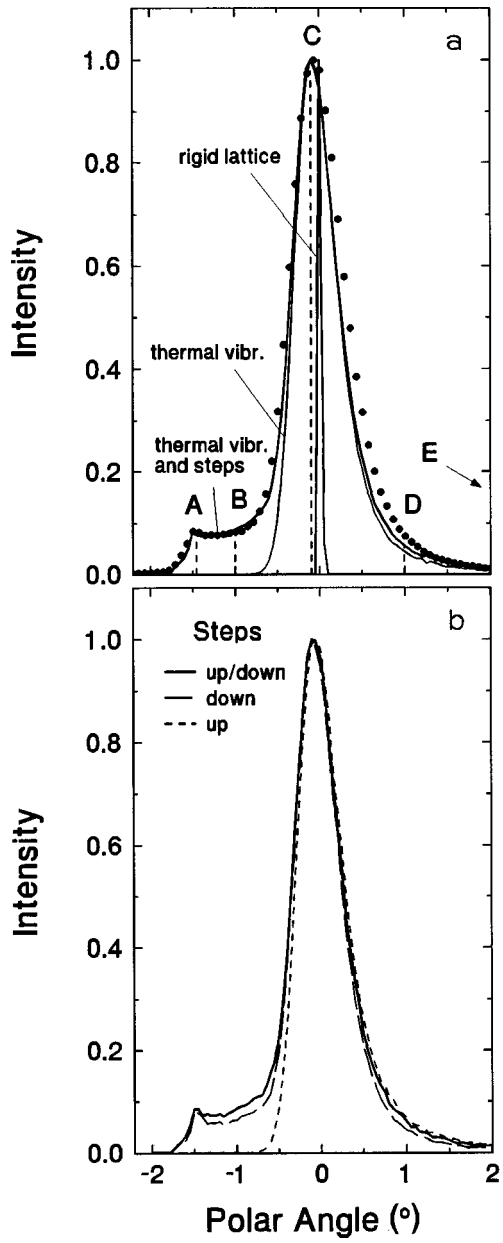

FIG. 4. (a) Measured (circles) and calculated (curves) polar angular distributions for scattering at (1) a perfect rigid surface lattice, (2) a perfect surface with thermally elongated atoms, and (3) a surface with thermal elongations and surface steps (mean step distance $s=500$ Å). $\Phi_{in}=1.75°$, $T=600$ K. Polar angles A–E correspond to trajectories shown in Fig. 5. (b) Calculated polar angular distributions for scattering at a surface with a random sequence of upward and downward steps ($s=500$ Å) [No. (3) from (a)], a surface with downward steps only ($s=1000$ Å), and a surface with upward steps only ($s=1000$ Å).

The simulation does not describe the foot structure observed at small scattering angles. In order to find the origin of this structure, we incorporate surface steps. We assume a random occurrence of steps without interaction between them. This implies a geometrical distribution function of terrace sizes.[46,47] Only monatomic steps are considered and upward and downward steps occur with equal probability. This reproduces the observed angular distributions well. The foot structure sets in at the edge of the shadow cast by the target ($\Phi=-\Phi_{in}$). The height of the plateau is given by the mean

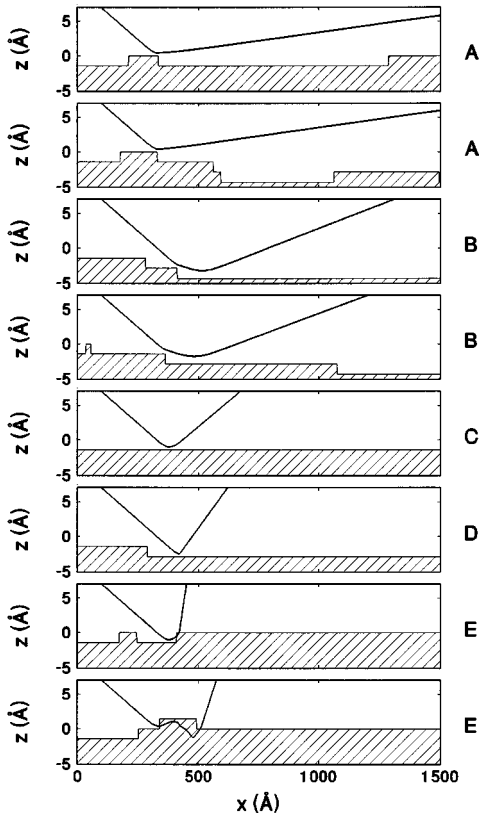

FIG. 5. Selection of ion trajectories leading to scattering at polar angles A–E from Fig. 4(a). $\Phi_{in}=1.75°$, $T=600$ K. Note the largely different scales of abscissa and ordinate.

distance between steps. Note that steps hardly contribute to the width of the distribution. Effects owing to thermal vibrations and surface steps on angular distributions thus do not interfere.

In Fig. 5 we plot typical projectile trajectories, which lead to scattering under polar angles marked A–E in Fig. 4(a). Particles interacting with a flat terrace are scattered into the maximum of the main peak (C) or, when largely elongated atoms are encountered, into the flanks (D). Particles which encounter a *downward* step are scattered subspecularly due to the sudden weakening of the repulsive potential when crossing the step edge. Then the particle is either reflected from a lower lying terrace (B) or directly scattered back (A). In contrast, projectiles hitting an *upward* step are scattered by large angles and do not contribute to measured angular distributions (E). The latter case may also lead to planar channeling below the surface layer (''subsurface channeling'') (E, bottom).[48]

In conclusion, the foot in the polar angular distribution is caused by *downward* steps. This is elucidated in Fig. 4(b), where simulations are displayed which consider only downward steps (dashed curve) or only upward steps (dotted curve). For upward steps the (normalized) distribution is the same as for the flat surface [cf. Fig. 4(a)]. The foot structure evolves only when downward steps are incorporated. We note that the slightly lower plateau results from the normalization. In case of a surface with upward and downward steps (solid curve) the maximum of the angular distribution is lower due to the loss of particles at *upward* steps, as has been already found by Mannami *et al.*[49]

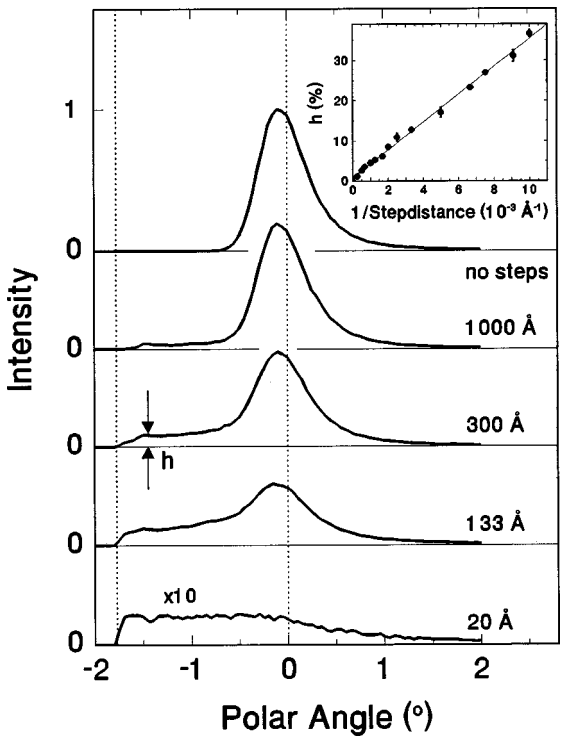

FIG. 6. Calculated polar angular distributions for different mean step distances s as indicated. $\Phi_{in}=1.75°$, $T=600$ K. All data are normalized to the maximum for the surface without steps. The height h of the foot in the polar angular distributions vs. inverse mean step distance s^{-1} (normalized to the maxima) is given in the inset.

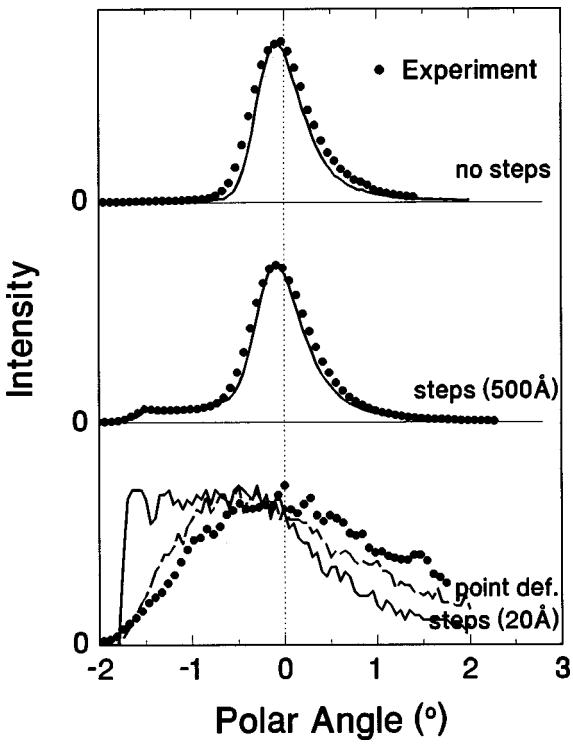

FIG. 7. Measured (circles) and simulated (curve) polar angular distributions for a surface annealed at 920 K (top), a surface annealed below 870 K (center), and a surface sputtered with 25 keV Ar^+ ions at 300 K (bottom). All distributions are normalized to their maxima.

We note that the footlike structure has a small peak in experiment and simulation (cf. Fig. 4). It is strongly dependent on the step height and has the characteristics of ''rainbow scattering,'' well known in other realms of atomic collision physics.[50] It will be discussed in detail in a forthcoming paper.[51]

In Fig. 6 angular distributions for different mean step distances s are shown. With increasing step density the foot structure increases and the maximum of the distribution decreases. As soon as the step distance s falls below the interaction length L, the height of the foot is comparable with the peak maximum, since the probability of hitting a surface step approaches 1. Obviously the height h of the foot is a measure of the step density. When h is plotted versus the inverse step distance s^{-1}, a linear relation is obtained (Fig. 6, inset). This is expected since the probability of hitting a step should be proportional to L/s for $s>L$.

In the experiment the surface step density can be chosen, within certain limits, by the preparation of the target, in particular the annealing temperature.[22] Typical polar angular distributions are shown in Fig. 7. The distributions for the flat (top) and the stepped surface (central) differ only in the height of the foot structure. In contrast the distribution for a sputtered surface consists of a single broad peak (bottom). Attempts to describe this by a simulation with a high step density fail (solid curve). Better agreement is found for a surface with point defects, modelled here by a high temperature (40000 K), corresponding to a rms displacement of half the Fe lattice constant (dashed curve).

B. Variation of the angle of incidence

Angular distributions for different incidence angles are displayed in Fig. 8. When Φ_{in} is increased, two trends are observed: (1) The distributions broaden and (2) their maxima shift to negative polar angles (''subspecular reflection'') (see inset in Fig. 8). Both trends are reproduced in the simulations. A broadening of the peaks is expected, since the projectiles increasingly feel thermal displacements at larger transverse energies. Subspecular reflection at larger transverse energy has been observed in Ref. 53 and may be explained by a diffusion approximation,[54] where the movement of a projectile owing to small-angle scattering is treated as a diffusion in the directions of its velocity. This implies that (some) projectiles penetrate the surface for larger transverse energies, which is in accordance with the simulation.

As anticipated the simulations fail to describe the experiment satisfactorily at small incidence angles. The observed angular distributions have considerable angular spreads and are shifted for small transverse energies to positive angles (''superspecular reflection''). This results from an acceleration of incident ions in their image potential,[55,56] which is not considered in the simulation.

Figure 9 shows the widths of angular distributions from experiment (full circles) and simulation. We plot the square of the full width at half maximum (FWHM), because this representation allows us to simply add contributions of separate processes in the case of Gaussian broadenings. The corrugation of the potential for the rigid lattice hardly contributes to the broadening (dotted curve). The same applies for surface steps (long-dashed curve). The main contribution to

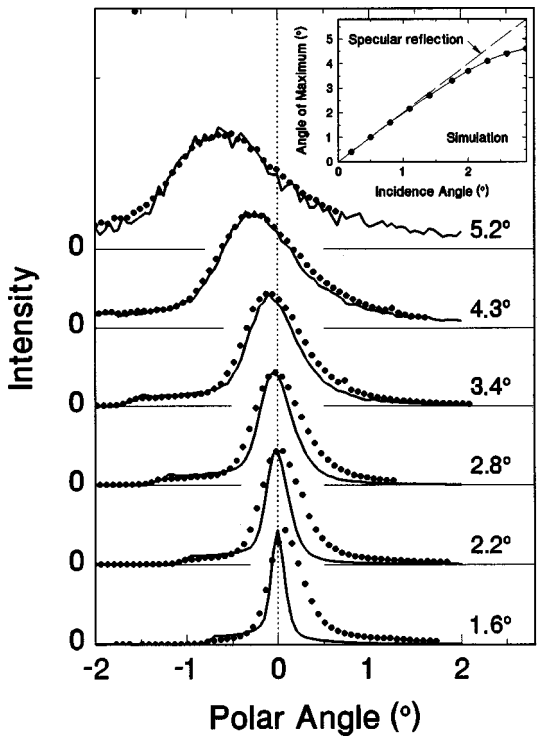

FIG. 8. Measured (circles) and simulated (curves) polar angular distributions for scattering angles Φ_s as indicated. The incidence angles Φ_{in} used in the simulation are 0.8°, 1.1°, 1.4°, 1.75°, 2.3°, and 2.9°, respectively, from bottom to top. $T=600$ K, $s=400$ Å. The data point in the upper left corner is from the direct beam for the distribution at $\Phi_s=1.6°$. Inset: most probable scattering angle Φ_s. The critical incidence angle for ''semiplanar surface channeling'' is 2.9° (Ref. 52).

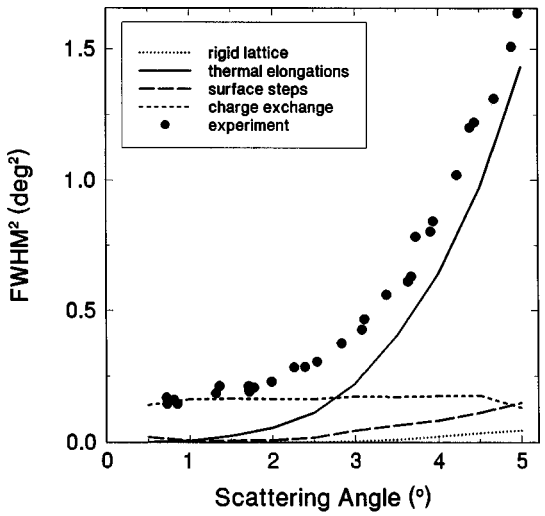

FIG. 9. FWHM^2 of measured (open circles) and simulated (curves) polar angular distributions vs scattering angle Φ_s. Long dashed curve: perfect rigid surface; dotted curve: rigid surface with steps ($s=400$ Å); solid curve: surface with thermal elongations ($T=600$ K) and steps ($s=400$ Å). Short dashed curve: difference between experiment (open circles) and solid curve.

the angular spread results from thermal elongations (solid curve). The residual deviation between experiment and simulation is constant and dominates for small incidence angles (short-dashed curve). This contribution may be attributed to electronic processes (e.g., multiple scattering by target electrons, image charge effects,[55] fluctuations in charge states of the projectiles[57]). Such processes, which are neglected in the simulation, seem to determine a lower limit in the angular spread for grazing scattering from a perfect surface.

C. Thermal elongations of surface lattice atoms

Grazing ion-surface scattering is a powerful technique to study the thermal behavior of surfaces due to its ability to separate effects of thermal elongations from those caused by surface steps. This feature is difficult to claim by other techniques such as x-ray diffraction, LEED, low-energy atom scattering, or double alignment medium-energy ion scattering. In this collision geometry the width of angular distributions does not depend on interlayer relaxations or in-plane thermal vibrations, but is sensitive to the normal component of thermal elongations of topmost layer atoms. This is shown in Fig. 10, where the FWHM^2 of the angular distribution is found to increase roughly linearly with temperature. Thus, according to Eq. (1), the angular spread scales linearly with the rms thermal displacement.

Measured angular distributions are shown in Fig. 11 as a function of temperature. At $T=473$ K the experiment is reproduced by the simulation, with a small residual deviation due to electronic processes (see Sec. IV B), which amounts to the same value as in Fig. 9. Yet the deviation increases with temperature. Since all simulations are performed with the same surface Debye temperature T_z, the thermal displacements at the highest temperatures seem to be larger than expected from the harmonic approximation. On the other hand, the height of the foot structure is reproduced at all

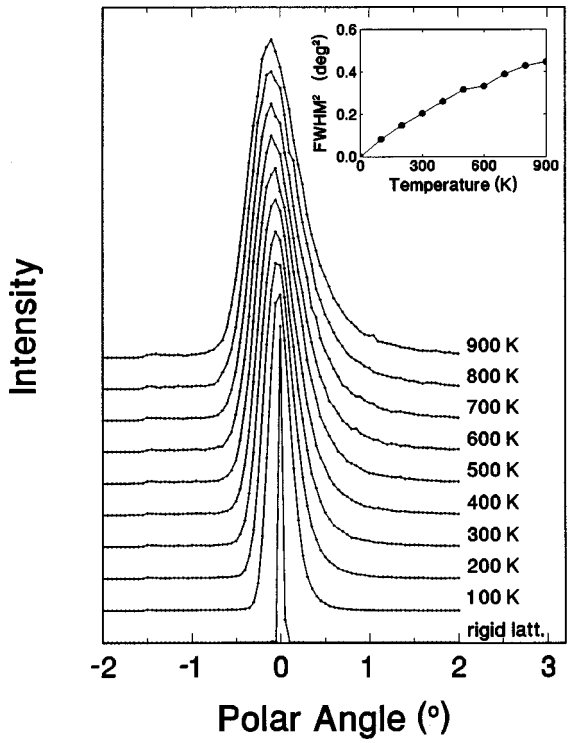

FIG. 10. Calculated polar angular distributions for $\Phi_{in}=1.75°$, $s=6000$ Å, and temperatures as indicated and their FWHM^2 (inset).

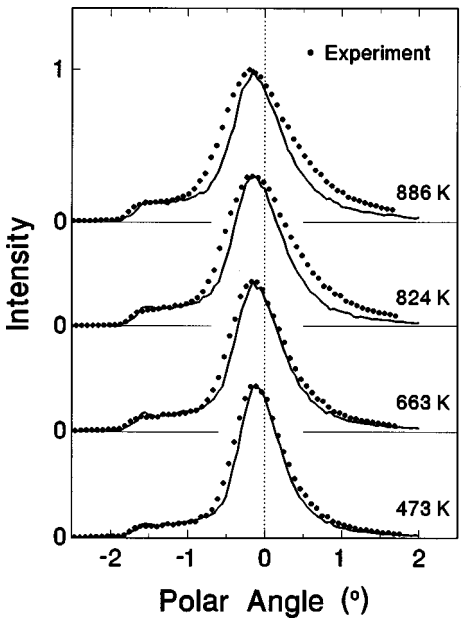

FIG. 11. Measured (circles) and simulated (curves) polar angular distributions for temperatures as indicated. $\Phi_{in}=1.85°$, $s=400$ Å. The simulations are performed for constant Debye temperature $T_z=227$ K (harmonic approximation).

temperatures. Hence the density of surface steps does not change. In particular, a proliferation of steps or roughening transition[58] can be excluded.

The FWHM of experiment (solid circles) and simulation (open symbols) are plotted in Fig. 12(a) as function of temperature T. The harmonic approximation (open circles) gives good agreement for temperatures up to 700 K. The increasing deviation at larger temperatures is interpreted by anharmonic vibrations. In order to quantify this anharmonicity, we adopt a quasiharmonic approach where the Debye temperature is chosen to be temperature dependent. A fit to the experimental data yields $T_z=215$ K at a surface temperature of 700 K, 200 K at 750 K, 180 K at 800 K, 170 K at 850 K, and 160 K at 900 K (open squares). The corresponding mean square displacements $\langle u_z^2\rangle$ are calculated from Eq. (1) and amount, e.g., to 916 pm^2 for 900 K, in contrast to 455 pm^2 as expected from the harmonic model.

Because anharmonicity and surface steps may be related,[59] we repeated the measurements for a flat surface (step distance >1000 Å). The results are shown in Fig. 12(b). They confirm the results obtained for the stepped surface, i.e., there is no indication of a direct or indirect (through adatoms originating from step edges) effect of the step density on the anharmonicity.

D. Submonolayer films

Studies on ultrathin epitaxial films require techniques to monitor and control growth in real time and *in situ*. Prominent techniques are reflection high-energy electron diffraction (RHEED),[60,61] x-ray diffraction,[62,63] or diffraction of thermal-energy atoms,[64,65] due to their excellent compatibility with molecular beam epitaxy. Conceptually similar is grazing ion-surface scattering, which has been applied to study semiconductor[66] and metal growth.[19] It allows one to determine the completion of individual atomic layers, characterize the growth mode, and evaluate the distribution and size of grown islands.[20,21] Though grazing ion-surface scattering does not give diffraction information such as, e.g., RHEED, it has the advantage of an ultimate surface sensitivity and, as discussed in the following, a straightforward interpretation.

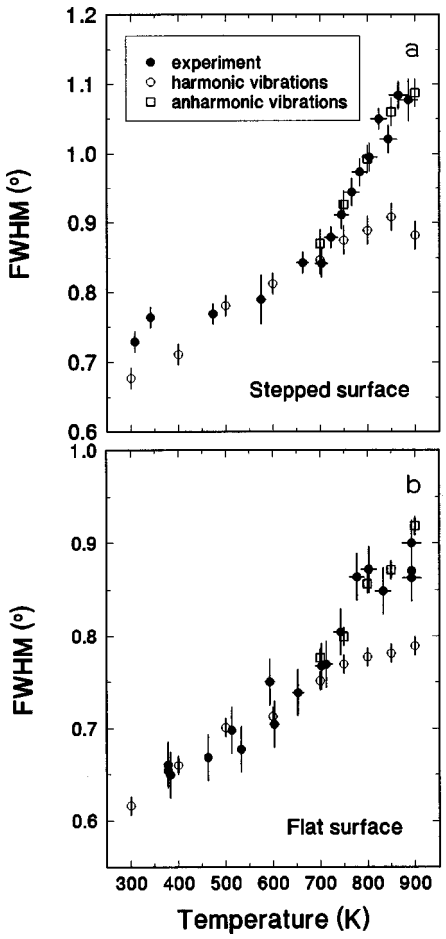

FIG. 12. (a) FWHM of measured (solid circles) and simulated (open symbols) polar angular distributions. $\Phi_{in}=1.85°$, $s=400$ Å. Open circles are results with thermal elongations from the harmonic model; open squares are best fit data for anharmonic vibrations. The simulated distributions have been convoluted to correct for broadening due to electronic processes. (b) Same as (a), but $\Phi_{in}=1.75°$ and $s=6000$ Å.

In Fig. 13 we display polar angular distributions recorded during submonolayer growth of Cr on Fe(001). The temperature is 300 K, where growth is known to be transient layer-by-layer.[67] When the clean surface is covered with 0.1 ML of Cr a pronounced decrease in the scattered intensity is observed. This behavior continues until, at about 0.4 ML, the intensity starts to increase again. The explanation is straightforward: at the beginning of growth the roughness rapidly increases due to nucleation of islands (nucleation regime[68]) and disturbs the correlated small angle scattering process. Upon further deposition the islands grow in size and the roughness further increases slowly (aggregation regime). It is maximal, when the layer is about half filled and decreases when completion of the layer is approached (coalescence and percolation regime).

In the computer simulation we assume that submonolayer growth is epitaxial and pseudomorph[20] and evolves from

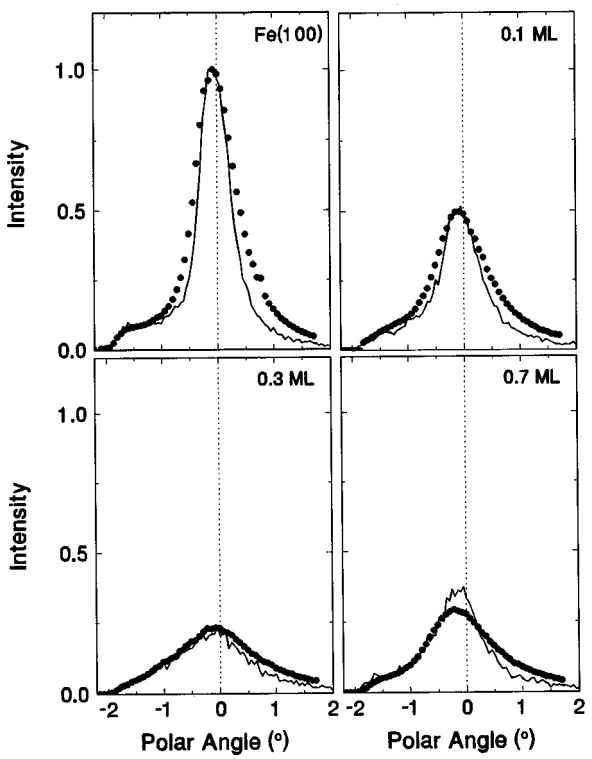

FIG. 13. Measured (circles) and simulated (curves) polar angular distributions for 25 keV He^+ ions scattered from clean and Cr covered Fe(001). $\Phi_{in}=1.9°$, $T=300$ K, and $s=300$ Å. All data are normalized to the maximum for the clean surface. The density of Cr islands is constant with a mean distance of 50 Å.

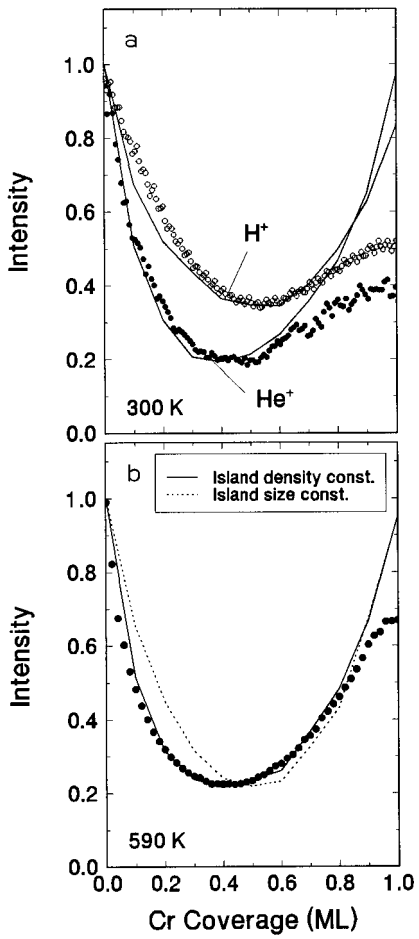

FIG. 14. (a) Intensity of reflected 25 keV H^+ and He^+ ions (open and solid circles, respectively) during growth of 1 ML Cr on Fe(001) at $T=300$ K. $\Phi_{in}=1.75°$. The simulation is performed with $s=600$ Å, and a constant density of Cr islands with a mean distance of 60 Å. (b) Intensity of reflected 25 keV He^+ ions during growth of 1 ML Cr on Fe(001) at $T=590$ K. The initial growth temperature was 340 K in order to artificially enhance the density of nuclei (Ref. 72). $\Phi_{in}=1.75°$. The simulations are fits to the data with constant mean island density (mean island distance 65 Å) and constant mean island size (mean island size 30 Å), respectively.

monolayer islands with a mean distance l and sizes according to the instantaneous coverage θ. We thus assume a constant island density (see below) and a negligible monomer density. As shown in Fig. 13, both overall shapes and intensities of the distributions are well described by the simulation for $l=60$ Å. The agreement is poorer for $\theta=0.7$ ML. This is expected, since we are in the middle of the coalescence and percolation regime,[68] where the island density changes and growth on top of islands sets in.

Most striking feature in Fig. 13 is the strong variation of the intensity of the maximum. In order to continuously monitor growth it is therefore sufficient to record the intensity in the maximum of the distribution as function of evaporation time or coverage, in analogy to the most common application of RHEED. An example is shown in Fig. 14(a), where growth of Cr is studied by scattering of He^+ (solid circles) and H^+ ions (open circles). According to the arguments given above, the intensity shows an oscillatory variation. This is reproduced in the simulation for sufficiently low coverages, where nucleation on top of islands is negligible. For coverages approaching 1 ML the measured intensities are lower than simulated showing that the monolayer film has holes and islands on top of it.

Note that the signal for He^+ scattering decays stronger. This is ascribed to the larger angular spread for H^+ projectiles due to the closer distance of approach to the surface, which results in a reduced sensitivity to changes in surface roughness.[20] The observed signals are reproduced by the simulations, which were performed with the same parameters (island distance, step distance, ion energy, incidence angle, etc.), according to the experiment. Only the atomic number of the projectile and, consequently, the interaction potential are changed.

RHEED oscillatons have been generally attributed to a temporal variation of the surface step density during growth.[69] Recently this step density model has been seriously questioned.[70] Calculations based on the dynamical theory show that an increased step density alone tends to produce an *increase* of the specularly reflected intensity rather than a decrease. This is opposite to grazing ion scattering, where steps always reduce the intensity of specularly reflected ions, as shown in Sec. IV A. Nevertheless it turns out that the intensity of specularly reflected ions is not only affected by the step density, but also by the coverage, which are *a priori* not correlated. Let us consider two limiting cases in two-dimensional growth: (1) constant mean island density and (2) constant mean island size. These models are incorporated in the simulation by a probability p_d of encountering a downward step from an island on the surface on going

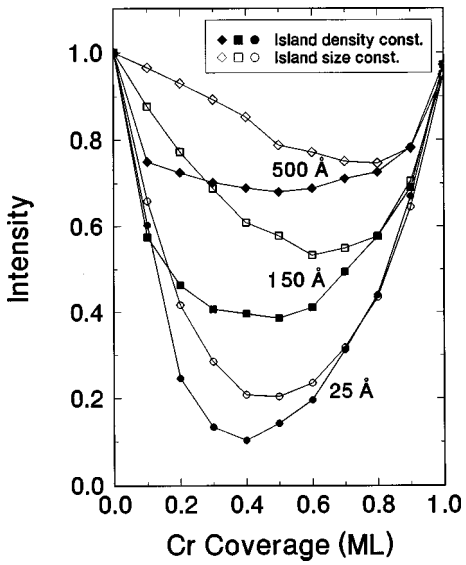

FIG. 15. Calculated intensity of reflected 25 keV He^+ ions vs coverage of Cr on Fe(001) for constant mean island density [model (1)] (solid symbols) and constant mean island size [model (2)] (open symbols), respectively. The mean island distance (1) or mean island size (2) is indicated. $\Phi_{in}=1.75°$, $T=600$ K, and $s=600$ Å.

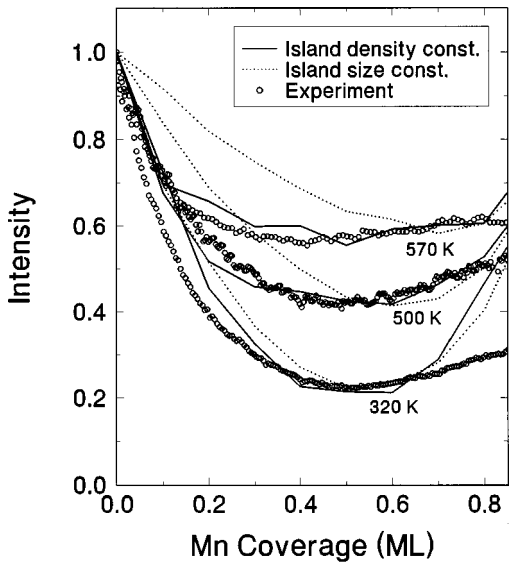

FIG. 16. Measured and calculated intensity of reflected 25 keV H^+ ions during growth of Mn on Fe(001) at temperatures as indicated. $\Phi_{in}=1.75°$. The simulation is performed with $s=1000$ Å, constant island density (mean island distance 250, 110, and 30 Å from top to bottom) and constant island size (mean island size 150, 60, and 15 Å).

from one lattice site to an adjacent one. Analogously, p_u denotes the probability for an upward step from an uncovered area on the surface. This produces a geometrical terrace size distribution[70,71] at a coverage

$$\theta=\frac{p_u}{p_d+p_u} \tag{2}$$

and a step density

$$\rho=\theta p_d+(1-\theta)p_u\,. \tag{3}$$

A constant mean island density [model (1)] is realized for

$$p_u=\frac{\rho}{2(1-\theta)} \tag{4}$$

and

$$p_d=\frac{\rho}{2\theta}, \tag{5}$$

where the step density ρ is used as parameter and determines the mean distance between islands (nucleation length) $l=2/\rho$.

A constant mean island size [model (2)] is obtained for

$$p_u=p_d\,\frac{\theta}{1-\theta}. \tag{6}$$

Here, the mean island size $1/p_d$ is used as parameter and the step density $\rho=2\,\theta p_d$ depends on the coverage.

Results for both models are presented in Fig. 15 for a mean island distance [model (1)] or a mean island size [model (2)] as indicated. Both models produce pronounced oscillations. In the case of a constant step density (solid symbols), the intensity of specularly reflected projectiles is obviously related to the surface roughness $\sigma=\langle[z(x_0)-\langle z(x_0)\rangle]^2\rangle^{1/2}$ (the average is over all positions x_0), which shows the same cusplike shape with a maximum at 0.5 ML for two-dimensional growth, corresponding to a minimum in the reflected intensity.

For constant island size (open symbols) the intensity minima are shifted to higher coverages. Thus it is the increasing step density which determines the intensity variations. Note that the minima are lower for smaller terraces, which we ascribe to a reduced height correlation $\Gamma(x)=\langle z(x_0)z(x_0+x)\rangle-\langle z(x_0)\rangle^2$. This is immediately realized, since, e.g., terraces which are much larger than the interaction length L do not disturb the correlated small angle scattering process at all.

Comparisons with experimental data are presented in Figs. 14(b) and 16 for growth of Cr and Mn on Fe(001). In both cases the constant island density model agrees well with our observations. This is in accordance with Monte Carlo calculations which show that nucleation of islands in epitaxial growth is already terminated during an early stage of growth.[68] Variation of the growth temperature in Fig. 16 shows that the nucleation length increases with temperature due to enhanced lateral diffusion.

V. SUMMARY

We have shown that scattering of light ions under a grazing angle from a single crystal surface is a direct and sensitive technique to study surface defects. The polar angular distribution of reflected ions is affected in a characteristic manner by the presence of defects at the topmost surface layer. The technique allows for a clear separation of contributions from one-, two-, and three-dimensional defects. Computer simulations based on the binary collision approximation permit a quantitative analysis of data.

The angular spreads of reflected ions are predominantly affected by thermal displacements of topmost surface layer

atoms. Measurements at a clean Fe(001) surface indicate that anharmonic vibrations of surface lattice atoms develop at about half the bulk melting temperature of Fe.

The effect of surface steps on the scattering process is twofold: *downward* steps produce a footlike structure in the angular distribution at small scattering angles. The relative intensity of this structure scales with the step density and can be calibrated by computer simulation. *Upward* steps generally lead to large-angle scattering and a consequent loss in intensity of ions scattered in forward directions.

Epitaxial growth of ultrathin films is monitored by recording the intensity of reflected ions. This enables one to obtain information on growth mode and quality of the film surface from computer simulations, such as, e.g., on the density and size of grown islands. Measurements for submonolayer growth of Cr and Mn on Fe(001) show that the density of islands is essentially constant over a wide range of coverages. The mean distance between islands sensitively depends on the growth temperature.

ACKNOWLEDGMENTS

The experimental part of this work has been performed in collaboration with Professor H. Winter and T. Igel. Assistance in running the experiments by K. Maass, R.-A. Noack, M. Ostwald, and P. Wolf is gratefully acknowledged. This work was supported by the Deutsche Forschungsgemeinschaft in Sonderforschungsbereich 290 and Project No. Wi1336.

*FAX: +49 30 2093 7899. Electronic address: pfandz@physik.hu-berlin.de

[1] M. Henzler, *Electron Spectroscopy for Surface Analysis*, edited by H. Ibach (Springer, Berlin, 1977), p. 117.

[2] *Low Energy Ion-Surface Interactions*, edited by J. W. Rabalais (Wiley, Chichester, 1994).

[3] *Inelastic Ion-Surface Collisions*, Proceedings of the Eleventh International Workshop on Inelastic Ion-Surface Collisions, Wangerooge, Germany, 1996, edited by W. Heiland and E. Taglauer [Nucl. Instrum. Methods Phys. Res. B **125**, 1 (1997)].

[4] N. Bohr, K. Dan, K. Dan. Vidensk. Selsk. Mat. Fys. Medd. **18**, 8 (1948).

[5] W. Eckstein, *Computer Simulation of Ion-Solid Interactions*, (Springer, Berlin, 1991).

[6] R. M. Logan and R. E. Stickney, J. Chem. Phys. **44**, 195 (1966).

[7] E. K. Grimmelmann, J. C. Tully, and M. J. Cardillo, J. Chem. Phys. **72**, 1039 (1980).

[8] J. C. Tully, J. Chem. Phys. **92**, 680 (1990).

[9] R. Smith and R. P. Webb, Nucl. Instrum. Methods Phys. Res. B **67**, 373 (1992).

[10] K. Gärtner, D. Stock, B. Weber, G. Betz, M. Hautala, G. Hobler, M. Hou, S. Sarite, W. Eckstein, J. J. Jiménez-Rodríguez, A. M. C. Pérez-Martín, E. P. Anribet, V. Konoplev, A. Gras-Marti, M. Posselt, M. H. Shapiro, T. A. Tombrello, H. M. Urbassek, H. Hensel, Y. Yamamura, and W. Takeuchi, Nucl. Instrum. Methods Phys. Res. B **102**, 183 (1995).

[11] D. M. Danailov, D. J. O'Connor, and K. J. Snowdon, Surf. Sci. **347**, 215 (1996).

[12] D. M. Danailov, J.-H. Rechtien, and K. J. Snowdon, Surf. Sci. **259**, 359 (1991).

[13] H. Sakai, R. Yamashita, and Y. O. Ohtsuki, Nucl. Instrum. Methods Phys. Res. B **96**, 494 (1995).

[14] H. Sakai, T. Iitaka, and Y. H. Ohtsuki, Phys. Lett. A **161**, 467 (1992).

[15] C. Höfner, A. Närmann, and W. Heiland, Nucl. Instrum. Methods Phys. Res. B **72**, 227 (1992).

[16] H. Derks, A. Närmann, and W. Heiland, Nucl. Instrum. Methods Phys. Res. B **44**, 125 (1989).

[17] R. Pfandzelter and J. W. Lee, Nucl. Instrum. Methods Phys. Res. B **45**, 641 (1990).

[18] Y. Fujii, K. Kimura, M. Hasegawa, M. Suzuki, Y. Susuki, and M. Mannami, Nucl. Instrum. Methods Phys. Res. B **33**, 405 (1988).

[19] T. Igel, R. Pfandzelter, and H. Winter, Europhys. Lett. **35**, 67 (1996).

[20] R. Pfandzelter, T. Igel, and H. Winter, Surf. Sci. **375**, 13 (1996).

[21] R. Pfandzelter, T. Igel, and H. Winter, Surf. Sci. **389**, 317 (1997).

[22] R. Pfandzelter, T. Igel, and H. Winter, Phys. Rev. B **56**, 14 948 (1997).

[23] W. Graser and C. Varelas, Phys. Scr. **T6**, 153 (1983).

[24] M. Schuster and C. Varelas, Surf. Sci. **134**, 195 (1983).

[25] C. Lehmann and G. Leibfried, Z. Phys. **172**, 465 (1963).

[26] C. Varelas and R. Sizmann, Radiat. Eff. **25**, 163 (1975).

[27] G. Molière, Z. Naturforsch. A **2**, 133 (1947).

[28] D. J. O'Connor and J. P. Biersack, Nucl. Instrum. Methods Phys. Res. B **15**, 14 (1986).

[29] R. J. Glauber, Phys. Rev. **98**, 1692 (1955).

[30] M. C. Desjonquères and D. Spanjaard, *Concepts in Surface Physics* (Springer, Berlin, 1993).

[31] D. P. Jackson, Surf. Sci. **43**, 431 (1974).

[32] T. Hecht (private communication).

[33] O. B. Firsov, Sov. Phys. JETP **6**, 534 (1958).

[34] J. F. Ziegler, J. P. Biersack, and U. Littmark, in *The Stopping and Range of Ions in Matter*, edited by J. F. Ziegler (Pergamon, New York, 1985), Vol. 1.

[35] R. Pfandzelter, F. Stölzle, H. Sakai, and Y. H. Ohtsuki, Nucl. Instrum. Methods Phys. Res. B **83**, 469 (1993).

[36] B. W. Dodson, Phys. Rev. B **36**, 1068 (1987).

[37] Y. H. Ohtsuki, K. Koyama, and Y. Yamamura, Phys. Rev. B **20**, 5044 (1979).

[38] K. J. Snowdon, D. J. O'Connor, and R. J. MacDonald, Phys. Rev. Lett. **61**, 1760 (1988).

[39] F. Stölzle and R. Pfandzelter, Phys. Lett. A **150**, 315 (1990).

[40] H. Winter and M. Sommer, Phys. Lett. A **168**, 409 (1992).

[41] T. Kurose, M. Kato, N. Inoue, T. Hasegawa, and K. Matsuzawa, Nucl. Instrum. Methods Phys. Res. B **67**, 320 (1992).

[42] P. M. Echenique, Nucl. Instrum. Methods Phys. Res. B **27**, 256 (1983).

[43] S. Ohnishi, A. J. Freeman, and M. Weinert, Phys. Rev. B **28**, 6741 (1983).

[44] C. Auth, A. Mertens, and H. Winter (unpublished).

[45] K. Kimura and M. Mannami, Nucl. Instrum. Methods Phys. Res. B **27**, 442 (1987).

[46] M. Henzler, Surf. Sci. **73**, 240 (1978).

[47] T.-M. Lu and M. G. Lagally, Surf. Sci. **120**, 47 (1982).

[48] K. Kimura, M. Hasegawa, and M. Mannami, Phys. Rev. B **36**, 7 (1987).

[49] M. Mannami, Y. Fujii, and K. Kimura, Surf. Sci. **204**, 213 (1988).

[50] A. W. Kleyn and T. C. M. Horn, Phys. Rep. **199**, 191 (1991).
[51] R. Pfandzelter, T. Igel, and H. Winter (unpublished).
[52] R. Sizmann and C. Varelas, Festkoerperprobleme **XVII**, 261 (1977).
[53] M. Wilke, Diploma thesis, Universität Münster, 1994.
[54] V. S. Remizovich, M. I. Ryazanov, and I. S. Tilinin, Sov. Phys. JETP **52**, 225 (1980).
[55] H. Winter, J. Phys.: Condens. Matter **8**, 10 149 (1996).
[56] H. Winter, Europhys. Lett. **18**, 207 (1992).
[57] M. Kato and K. J. Snowdon, Nucl. Instrum. Methods Phys. Res. B **90**, 80 (1994).
[58] E. H. Conrad, Prog. Surf. Sci. **39**, 65 (1992).
[59] B. Loisel, J. Lapujoulade, and V. Pontikis, Surf. Sci. **256**, 242 (1991).
[60] J. J. Harris, B. A. Joyce, and P. J. Dobson, Surf. Sci. **103**, L90 (1981).
[61] S. T. Purcell, B. Heinrich, and A. S. Arrott, Phys. Rev. B **35**, 6458 (1987).
[62] E. Vlieg, A. W. Denier van der Gon, J. F. van der Veen, J. E. Macdonald, and C. Norris, Phys. Rev. Lett. **61**, 2241 (1988).
[63] P. H. Fuoss, D. W. Kisker, F. J. Lamelas, G. B. Stephenson, P. Imperatori, and S. Brennan, Phys. Rev. Lett. **69**, 2791 (1992).
[64] L. J. Gómez, S. Bourgeal, J. Ibáñez, and M. Salmerón, Phys. Rev. B **31**, 2251 (1985).
[65] R. Kunkel, B. Poelsema, L. K. Verheij, and G. Comsa, Phys. Rev. Lett. **65**, 733 (1990).
[66] Y. Fujii, K. Narumi, K. Kimura, M. Mannami, T. Hashimoto, K. Ogawa, F. Ohtani, T. Yoshida, and M. Asari, Appl. Phys. Lett. **63**, 2070 (1993).
[67] D. T. Pierce, J. A. Stroscio, J. Unguris, and R. J. Celotta, Phys. Rev. B **49**, 14 564 (1994).
[68] J. G. Amar, F. Family, and P.-M. Lam, Phys. Rev. B **50**, 8781 (1994).
[69] S. Clarke and D. D. Vvedensky, Phys. Rev. Lett. **58**, 2235 (1987).
[70] U. Korte and P. A. Maksym, Phys. Rev. Lett. **78**, 2381 (1997).
[71] C. S. Lent and P. I. Cohen, Surf. Sci. **139**, 121 (1984).
[72] G. Rosenfeld, B. Poelsema, and G. Comsa, J. Cryst. Growth **151**, 230 (1995).